

## MODELING THE ACCRETION STRUCTURE OF AU Mon

CORWIN ATWOOD-STONE<sup>1,2</sup>, BRENDAN P. MILLER<sup>1,3</sup>, MERCEDES T. RICHARDS<sup>4</sup>, JÁN BUDAJ<sup>5</sup>, AND GERALDINE J. PETERS<sup>6</sup>

<sup>1</sup> Department of Physics, College of Wooster, Wooster, OH 44691, USA

<sup>2</sup> Lunar and Planetary Laboratory, University of Arizona, Tucson, AZ 85721, USA; [catwoods@lpl.arizona.edu](mailto:catwoods@lpl.arizona.edu)

<sup>3</sup> Department of Astronomy, University of Michigan, Ann Arbor, MI 48109, USA; [mbrendan@umich.edu](mailto:mbrendan@umich.edu)

<sup>4</sup> Department of Astronomy & Astrophysics, Pennsylvania State University, University Park, PA 16802, USA; [mrichards@astro.psu.edu](mailto:mrichards@astro.psu.edu)

<sup>5</sup> Astronomical Institute, Slovak Academy of Sciences, Tatranska Lomnica 05960, Slovak Republic; [budaj@ta3.sk](mailto:budaj@ta3.sk)

<sup>6</sup> Space Sciences Center and Department of Physics & Astronomy, University of Southern California, Los Angeles, CA 90089-1341, USA; [gjpeters@mucen.usc.edu](mailto:gjpeters@mucen.usc.edu)

Received 2012 July 27; accepted 2012 October 17; published 2012 November 16

### ABSTRACT

AU Mon is a long-period (11.113 days) Algol-type binary system with a persistent accretion disk that is apparent as double-peaked H $\alpha$  emission. We present previously unpublished optical spectra of AU Mon which were obtained over 20 years from 1991–2011 with dense orbital phase coverage. We utilize these data, along with archival UV spectra, to model the temperature and structure of the accretion disk and the gas stream. Synthetic spectral profiles for lines including H $\alpha$ , H $\beta$ , and the Al III and Si IV doublets were computed with the *Shellspec* program. The best match between the model spectra and the observations is obtained for an accretion disk of inner/outer radius 5.1/23  $R_{\odot}$ , thickness of 5.2  $R_{\odot}$ , density of  $1.0 \times 10^{-13}$  g cm $^{-3}$ , and maximum temperature of 14,000 K, along with a gas stream at a temperature of  $\sim 8000$  K transferring  $\sim 2.4 \times 10^{-9} M_{\odot}$  yr $^{-1}$ . We show H $\alpha$  Doppler tomograms of the velocity structure of the gas, constructed from difference profiles calculated through sequentially subtracting contributions from the stars and accretion structures. The tomograms provide independent support for the *Shellspec* modeling, while also illustrating that residual emission at sub-Keplerian velocities persists even after subtracting the disk and stream emission. Spectral variability in the H $\alpha$  profile beyond that expected from either the orbital or the long-period cycle is present on both multi-week and multi-year timescales, and may reflect quasi-random changes in the mass transfer rate or the disk structure. Finally, a transient UV spectral absorption feature may be modeled as an occasional outflow launched from the vicinity of the disk–stream interaction region.

*Key words:* accretion, accretion disks – binaries: eclipsing – circumstellar matter – line: profiles – stars: imaging – stars: individual (AU Mon,  $\beta$  Lyr, CX Dra, SS Cyg, TT Hya, V393 Sco)

*Online-only material:* color figures

### 1. INTRODUCTION

Algol-type eclipsing binary systems consist of semi-detached components in which the secondary has evolved to overflow its Roche lobe. The current mass ratio results from the transfer of sufficient material onto the less-evolved primary until it was transformed into the more massive of the two stars (Crawford 1955; Kopal 1955). The relative separation of the components, the radius of the primary, and the mass ratio determine the types of accretion structures that eventually form. In short-period Algols ( $P \lesssim 4.5$  days), the gas stream arising from the L1 point can impact the gainer directly; in long-period systems ( $P \gtrsim 6$  days), the curving gas stream may instead feed into a stable disk; and in intermediate-period systems mixed behavior has been observed (e.g., Peters 1989; Richards & Albright 1999 and references therein). Secondary structures such as hot spots, outflows (potentially including jets), or accretion annuli can also develop. AU Mon (GCRV 4526, HD 50846, HIP 33237), with an orbital period of 11.113 days, has one of the longer periods among the well-studied Algol-type binaries (Richards & Albright 1999; Desmet et al. 2010), and is consequently ideally suited for investigation of the properties of an enduring accretion disk (even though it is sometimes variable), along with those of the gas stream and other accretion structures.

The components of Algol-type binary systems are typically too close to resolve as individual stars. A notable exception is the bright and nearby system of Algol ( $\beta$  Per) for which optical interferometry was used recently to resolve all three stars in that system (Zavala et al. 2010), with orbital parameters confirmed

and refined by radio interferometry (Peterson et al. 2011). These direct imaging techniques are still not able to resolve any of the non-stellar components including the accretion disk and gas stream. Instead, the non-stellar components can be revealed more readily with spectroscopy by disentangling the contributions of the stars from the composite spectrum. The receding/approaching sides of an accretion disk manifest as red/blueshifted emission superposed on the stellar absorption line profile, as first noted by Joy (1942). The persistent presence of double-peaked H $\alpha$  emission in the composite spectrum serves as one of the more prominent observational indicators of an enduring accretion disk. Additional accretion features, such as the gas stream, also influence the spectral profile to a lesser extent (e.g., as excess redshifted absorption when the viewpoint is through the stream, and as emission when viewed across the stream). A two-dimensional (2D) velocity mapping of the gas in the stream and disk may be constructed through Doppler tomography of the line profiles obtained at orbital phases around the binary (e.g., Marsh & Horne 1988; review by Richards 2004 and references therein). This technique has been extended to provide three-dimensional (3D) velocity maps (e.g., Agafonov et al. 2009; Richards et al. 2010, 2012). Hydrodynamic simulations provide another method of investigating the distribution of accreting gas, and can reproduce many of the features seen in the tomograms (Richards & Ratliff 1998; Bisikalo & Kononov 2010; Raymer 2012).

A complementary approach involves computing the spectral contribution from geometric representations of the accretion structures, so that the physical characteristics of the disk, stream,

or other features (size scales, density, temperature) may be determined through matching the modeled synthetic spectra to the observations. In this work, we make use of the *Shellspec* program developed by Budaj & Richards (2004). Briefly, this program calculates the line-of-sight radiative transfer within the moving circumstellar environment, and the stars can have Roche model geometries. For a given set of phases, a composite spectrum of the interacting binary is calculated with associated accretion structures: optionally including an accretion disk, a gas stream, a spot, a jet, and a shell. Consideration of multiple transitions helps to break potential parameter space degeneracies in modeling. Since Algol-type binaries frequently display variable line profiles, plausibly due to changes in the rate of mass transfer (e.g., Plavec & Polidan 1976; Richards & Albright 1999; Richards 2004), the parameters determined from the comparison of models with the data at a particular epoch describe the then-dominant accretion mode, and multi-epoch observations are required to explore the full range of conditions occurring within the system.

*Shellspec* provides a flexible framework for modification and extension to related astrophysical topics; for example, Tkachenko et al. (2009, 2010) created an inverted version of the code to determine properties of the component stars; Budaj (2011a) described an improved consideration of the reflection effect in *Shellspec* which he applied to modeling the temperature distribution over the surface of transiting exoplanets; Budaj (2011b) used *Shellspec* to model dust disks in  $\epsilon$  Aur; and Chadima et al. (2011) used *Shellspec* along with ZEUS-MP hydrodynamic models to illustrate the phase-varying H $\alpha$  V/R asymmetry resulting from injection of a blob of gaseous material (such as could occur from discontinuous mass transfer prior to viscosity-driven smoothing).

The current version of *Shellspec* applies a straight cylindrical representation of the gas stream and a circularly symmetric accretion disk, and the user may upload a general 3D accretion structure with optional velocity, temperature, and density fields (see [www.astro.sk/~budaj/shellspec.html](http://www.astro.sk/~budaj/shellspec.html)). Accretion disks in Algol-type binaries have often been suggested to lack circular symmetry or to possess regions of enhanced emission beyond that expected from a symmetric disk (e.g., the asymmetric disk model applied to RY Per by Barai et al. (2004), although their method did not include radiative transfer). *Shellspec* modeling of the accretion structures in TT Hya by Budaj et al. (2005) and Miller et al. (2007) demonstrated that the observed spectra could not be reproduced solely by the gas stream and a symmetric disk. In these cases, *Shellspec* can reproduce the observed characteristics through inclusion of the “spot” feature.

In this work, we investigate the partially eclipsing long-period Algol-type binary AU Mon. Comprehensive studies of the components of AU Mon based on *CoRoT* photometry were recently performed by Desmet et al. (2010) and Djurašević et al. (2010), with the former work including high-resolution spectroscopy to help constrain the stellar properties and the latter work additionally modeling the accretion disk; we use their results for system elements. Prior determinations of system parameters were made by Sahade et al. (1997) and Vivekananda Rao & Sarma (1998), and values for the ephemeris and period of AU Mon were derived by Lorenzi (1980) and Kreiner (2004). As in many Algol-type binary systems, the primary is carbon-poor, presumably due to deposition of CNO-processed material (Ibanoglu et al. 2012). Double-peaked H $\alpha$  emission has been seen in all observations (e.g., Plavec & Polidan 1976; Peters 1989; Sahade et al. 1996, 1997; Richards & Albright 1999;

Desmet et al. 2010; Barría & Mennickent 2011) with a profile that may vary between epochs (e.g., Plavec & Polidan 1976; Sahade et al. 1997). Peters & Polidan (1998) inferred a particle density in the disk of  $10^8$ – $10^9$  cm $^{-3}$  based on an examination of FUV Fe III features. Peters & Polidan (1984, 1998) found evidence from UV spectra of a high-temperature accretion region (HTAR) in several Algol-type binaries, including AU Mon. They determined that the HTAR was located near the trailing hemisphere of the primary (i.e., in the vicinity of the impact region where the gas stream collides with the stellar surface), with an electron temperature and density of around  $T_e = 10^5$  K and  $n_e = 10^9$  cm $^{-3}$ , and was carbon depleted (which suggested prior CNO processing of this material). Most recently, Djurašević et al. (2010) re-analyzed *CoRoT* and V-band photometry using a Roche model with a non-transparent accretion disk. They found that a “hot spot” and two “bright spots” (associated with spiral arms or deviations from a circular shape) account for the observed asymmetry in the light curve of AU Mon. We discuss their model in more detail in Section 3.1. Mimica & Pavlovski (2012) also used *CoRoT* photometry to independently characterize the disk of AU Mon as possessing a “clumpy” structure.

AU Mon was discovered by Lorenzi (1980) to display a long-period variation in brightness of  $\sim 0.2$  mag, with a period of  $\sim 417$  days (or 37.5 times the orbital period). This characteristic has now been associated with the Double Periodic Variables (DPVs; Mennickent et al. 2003) that show two photometric periods, one associated with orbital motion and the other a cyclic long-term light modulation that is about 35 times the orbital period. These systems tend to be more luminous than classical Algols and are categorized by mass loss and circumbinary disks in addition to mass transfer between stars; hence, they can be used to provide constraints on non-conservative models of binary star evolution (Mennickent et al. 2008). AU Mon was one of the first DPV systems discovered in our Galaxy within the class of Algol-type binaries; its properties will be compared with V393 Sco, a recently discovered DPV system (Mennickent et al. 2010).

Desmet et al. (2010) found that the shape of the light curves of AU Mon during long-period maxima and minima are identical but offset, and suggested that the intensity variations are instead linked to changes in the attenuation from circumbinary material; this interpretation is in agreement with Djurašević et al. (2010). Mennickent et al. (2008) hypothesized that variable mass outflow alters the amount of circumbinary material in DPVs, and Mennickent et al. (2010) associated the long-period variability in V393 Sco with equatorial mass loss. However, Peters (1994) found that the UV absorption associated with the gas stream was stronger when the stars were faint, and ascribed the long-period variation to changes in the mass transfer rate due to cyclic expansion and contraction of the secondary. Consistent with this, Barría & Mennickent (2011) showed that the H $\alpha$  and H $\beta$  central absorption in AU Mon is likewise deeper near and following minimum light, and concluded that the profile variability may result from a changing circumprimary envelope influenced by mass loss through the L1 point.

This paper is organized as follows: Section 2 describes the data and observations, including previously unpublished high-resolution optical spectra of AU Mon; Section 3 contains the *Shellspec* modeling process and the calculated characteristics of the accretion features; Section 4 considers spectral variability in AU Mon on both multi-year and multi-week timescales; Section 5 presents the Doppler tomography results based on

**Table 1**  
Optical Observations

ID <sup>a</sup>	HJD	$\phi_L$	$\phi_0$	$I_{\text{abs}}$	$I_{\text{blue}}$	$I_{\text{red}}$
KPNO1	2446122.728	7.24	298.870	0.96	1.17	1.17
	2446734.952	8.71	353.961	0.59	1.13	1.22
	2446734.862	8.71	353.952	0.59	1.09	1.21
	2446902.661	9.11	369.052	0.72	1.27	1.16
	2446903.663	9.11	369.142	1.05	1.26	1.22
	2446905.643	9.12	369.320	1.09	1.27	1.27
	2446919.634	9.15	370.579	1.00	1.25	1.28
	2447033.970	9.42	380.868	0.76	1.17	1.24
	2447469.840	10.47	420.089	0.48	1.19	1.10
	2447470.931	10.47	420.187	0.65	1.14	1.10
	2447471.868	10.47	420.272	0.70	1.13	1.10
	2447472.878	10.48	420.362	0.68	1.10	1.16
	2447560.669	10.69	428.262	0.78	1.28	1.19
	2447561.755	10.69	428.360	0.81	1.21	1.25
	2447636.645	10.87	435.099	0.94	1.31	1.15
	2447639.632	10.88	435.368	1.08	1.26	1.26
	2447640.637	10.88	435.458	1.04	1.25	1.24
	2447939.662	11.60	462.366	0.70	1.08	1.14
	2447939.778	11.60	462.376	0.66	1.11	1.19
	2447940.780	11.60	462.466	0.66	1.14	1.17
	2447941.593	11.60	462.539	0.70	1.08	1.18
	2447981.716	11.70	466.150	0.81	1.08	1.08
	2447983.615	11.70	466.321	0.85	1.11	1.11
	2448121.971	12.03	478.771	1.04	1.37	1.23
	2448123.959	12.04	478.950	0.82	1.20	1.28
	2448124.982	12.04	479.042	0.71	1.38	1.19
	2448125.985	12.04	479.132	1.05	1.35	1.23
	2448313.706	12.49	496.024	0.34	1.41	1.17
	2448313.792	12.49	496.032	0.35	1.34	1.07
	2448313.642	12.49	496.018	0.33	1.45	1.21
	2448314.754	12.50	496.118	0.59	1.26	1.18
	2448314.634	12.50	496.107	0.56	1.25	1.16
	2448318.688	12.51	496.472	0.53	1.24	1.25
	2448318.621	12.51	496.466	0.56	1.27	1.24
	2448319.764	12.51	496.569	0.63	1.23	1.30
	2448319.764	12.51	496.569	0.63	1.23	1.30
	2448320.619	12.51	496.646	0.67	1.27	1.19
	2448321.616	12.51	496.736	0.69	1.17	1.21
	2448514.977	12.98	514.135	1.01	1.30	1.19
	2449058.775	14.28	563.068	0.64	1.34	1.24
2449061.776	14.29	563.338	0.84	1.31	1.29	
2449443.708	15.20	597.706	0.99	1.21	1.22	
2449444.690	15.20	597.795	1.03	1.19	1.14	
2449688.900	15.79	619.770	0.86	1.18	1.23	
2449688.987	15.79	619.778	0.91	1.18	1.24	
2449689.048	15.79	619.783	0.94	1.18	1.24	
KPNO2	2449689.767	15.79	619.848	0.94	1.19	1.29
	2449689.856	15.80	619.856	0.93	1.18	1.29
	2449689.961	15.80	619.865	0.88	1.19	1.26
	2449690.055	15.80	619.874	0.77	1.17	1.24
	2449690.792	15.80	619.940	0.65	1.12	1.31
	2449690.901	15.80	619.950	0.61	1.11	1.32
	2449691.003	15.80	619.959	0.59	1.18	1.31
	2449691.051	15.80	619.963	0.58	1.15	1.34
	2449694.967	15.81	620.316	0.91	1.24	1.18
	2449695.048	15.81	620.323	0.88	1.24	1.19
	2450129.603	16.85	659.426	0.95	1.23	1.20
	2450129.641	16.85	659.430	0.95	1.24	1.20
	2450129.828	16.85	659.447	0.94	1.25	1.23
	2450130.638	16.85	659.519	0.89	1.21	1.30
	2450130.747	16.85	659.529	0.91	1.21	1.29
	2450130.830	16.85	659.537	0.91	1.18	1.28
	2450130.880	16.85	659.541	0.92	1.15	1.29
	2450131.624	16.85	659.608	1.02	1.21	1.28
	2450131.729	16.85	659.618	1.01	1.22	1.31

**Table 1**  
(Continued)

ID <sup>a</sup>	HJD	$\phi_L$	$\phi_0$	$I_{\text{abs}}$	$I_{\text{blue}}$	$I_{\text{red}}$
	2450131.828	16.86	659.626	1.02	1.23	1.29
	2450131.872	16.86	659.630	1.01	1.24	1.30
	2450132.639	16.86	659.699	0.97	1.26	1.25
KPNO3	2451191.906	19.40	755.017	0.42	1.37	1.25
	2451193.934	19.40	755.199	0.67	1.29	1.18
	2451196.898	19.41	755.466	0.46	1.19	1.17
	2451502.956	20.14	783.007	0.74	1.47	1.54
	2451503.997	20.15	783.100	1.02	1.29	1.22
	2451505.005	20.15	783.191	1.10	1.34	1.23
	2451510.890	20.16	783.721	1.05	1.31	1.22
	2451913.685	21.13	819.966	0.69	1.20	1.21
	HET	2452610.824	22.80	882.697	0.81	1.24
2452614.898		22.81	883.064	0.59	1.31	1.06
2452616.812		22.82	883.236	0.79	1.26	1.16
2452618.823		22.82	883.417	0.70	1.26	1.20
2452618.906		22.82	883.425	0.67	1.25	1.18
2452619.817		22.82	883.507	0.60	1.22	1.25
2452619.906		22.82	883.515	0.60	1.20	1.27
2452620.898		22.83	883.604	0.70	1.23	1.24
2452621.888		22.83	883.693	0.81	1.25	1.21
2452622.882		22.83	883.782	0.82	1.16	1.17
2452633.879		22.86	884.772	0.86	1.13	1.16
2452635.869		22.86	884.951	0.54	1.10	1.25
2452636.858		22.86	885.040	0.49	1.24	1.02
2452637.754		22.87	885.121	0.79	1.23	1.15
2452639.772		22.87	885.302	0.89	1.20	1.14
2452640.765		22.87	885.392	0.88	1.22	1.22
2452641.771	22.88	885.482	0.83	1.22	1.21	
2452642.851	22.88	885.579	0.88	1.15	1.26	
2452643.750	22.88	885.660	0.87	1.23	1.18	
2452644.754	22.88	885.751	0.95	1.17	1.13	
2452645.764	22.89	885.841	0.98	1.17	1.18	
2452649.739	22.89	886.199	0.88	1.22	1.11	
2452651.804	22.90	886.385	0.89	1.25	1.17	
2452652.710	22.90	886.466	0.81	1.22	1.20	
MDM	2455614.724	30.01	1163.046	0.44	1.38	1.15
	2455615.636	30.01	1163.131	0.61	1.16	1.12
	2455617.678	30.01	1163.312	0.87	1.14	1.06
	2455618.651	30.02	1163.400	0.83	1.13	1.14
	2455620.846	30.02	1163.597	0.65	1.12	1.13
LCO	2455878.823	30.64	1186.766	0.78	1.15	1.08

**Notes.** The long-period phase  $\phi_L$  is calculated from Equation (3) of Desmet et al. (2010) and the binary photometric phase  $\phi_0$  is calculated from Equation (2) of Desmet et al. (2010) but with the epoch shifted by 1030 periods. The quantities  $I_{\text{abs}}$ ,  $I_{\text{blue}}$ , and  $I_{\text{red}}$  provide the normalized flux level of the deepest H $\alpha$  central absorption and of the maximum H $\alpha$  emission in the blue and red wings.

<sup>a</sup> Data sets KPNO1 and KPNO3 were collected by Peters at KPNO; KPNO2 and HET were collected by Richards at KPNO and HET, respectively; MDM and LCO were collected by Miller and Atwood-Stone.

both observed and difference spectra, including comparisons between the observed spectra and the *Shellspec* model of the stars, disk, gas stream, and a high-density localized region (LR); Section 6 provides a summary of our results.

## 2. OBSERVATIONS

The 95 high-resolution optical spectra of AU Mon which form the primary focus of this work were collected at four observatories over a period of 20 years from 1991 to 2011: Kitt Peak National Observatory (KPNO), Hobby–Eberly Telescope (HET), MDM Observatory at Kitt Peak, and Las Campanas Observatory (LCO). (The MDM Observatory is operated by

a consortium of five universities: the University of Michigan, Dartmouth College, the Ohio State University, Columbia University, and Ohio University.) These observations are presented here for the first time, with the exception of 13 KPNO spectra. The observations are listed in Table 1.

Seventy-two  $H\alpha$  spectra of AU Mon were obtained at KPNO during several observing runs from 1991 to 2001. Most of these spectra were obtained with the 0.9 m Coudé Feed Telescope using grating A, providing a resolution of  $R \simeq 20,000$  across a spectral field of  $\sim 345 \text{ \AA}$ . Of these spectra, 13 were obtained in 1994 by Richards and were previously described in Richards & Albright (1999). In addition, 24 HET spectra were obtained with the HET High-Resolution Spectrograph (HRS) over 42 nights in 2002 December and 2003 January, with the 316g5936 cross disperser at a resolution of  $R = \lambda/\Delta\lambda \simeq 30,000$  and cover 4200–8000  $\text{\AA}$ . The HET spectra include both the  $H\alpha$  and the  $H\beta$  regions. Finally, six current-epoch spectra were obtained at MDM observatory (five  $H\alpha$  spectra, 2011 February) and at Las Campanas (one optical spectrum, 2011 November). The MDM  $H\alpha$  spectra were obtained with the 2.4 m Hiltner telescope using the Boller and Chivens CCD Spectrograph with the 1800 grating, providing a resolution of  $R \simeq 7500$  across a spectral field of  $\sim 330 \text{ \AA}$ , and the LCO optical spectra were obtained with the 6.5 m Clay Magellan telescope using the Magellan Inamori Kyocera Échelle double-Échelle spectrograph, providing a resolution of  $R \simeq 30,000$  near  $H\alpha$ .

The optical data were reduced using the Image Reduction and Analysis Facility (IRAF) following standard methods, briefly outlined below. This description applies to the HET data; while some specific details necessarily differed across the various telescopes and instruments, the general process was the same. Bias frames were averaged and then subtracted from the object and calibration frames. Flat fields were mode scaled and then median combined, then the master flat was normalized to remove the blaze function both along and across the dispersion axis, leaving only pixel-to-pixel variation; object frames were then divided by the normalized master flat. For each object image, obvious cosmic rays near/in the aperture were identified through inspection and removed through interpolation across columns (where the dispersion is approximately along rows). Next, the aperture was independently defined and traced for each image, and the one-dimensional spectra were extracted using a variance-weighted sum to minimize noise, with additional cosmic ray and bad pixel rejection performed using  $\sigma$  clipping. The dispersion relation was determined from a ThAr lamp spectrum obtained near the time of the object exposures. The spectra were normalized using a Chebyshev function with the  $H\alpha$  region excluded from the fit and the rejection  $\sigma$  set significantly lower for points below the curve (to minimize the influence of sharp absorption lines). The spectra were corrected to the heliocentric frame and then to the rest frame of the binary system, assuming the systemic velocity  $\gamma = 17.8 \text{ km s}^{-1}$  given by Desmet et al. (2010, their Table 8). Telluric atmospheric water vapor lines within the  $H\alpha$  region were removed with a model generated from a rapidly rotating standard star. The model was adjusted to match each observation by scaling the depth of the telluric absorption features to account for changes in airmass or other atmospheric variations; here, the line ratios of the telluric lines near  $H\alpha$  were assumed to be constant. When necessary, minor shifts in the model wavelengths were also made. Finally, any remaining obvious instrumental or cosmic ray artifacts were corrected by interpolating across neighboring non-affected pixels.

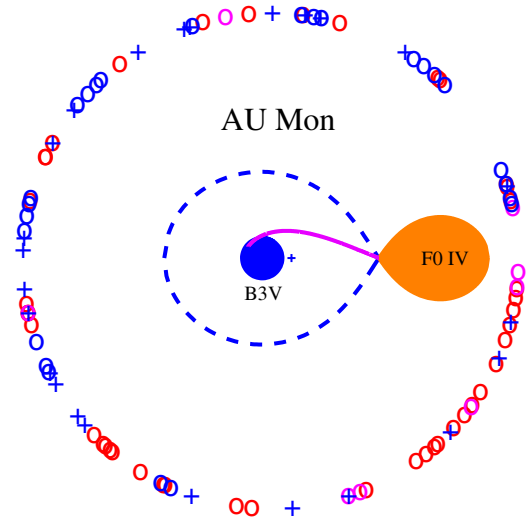


**Figure 1.** Geometry and phase coverage of AU Mon (see also Table 1). The dotted blue line is the primary’s Roche lobe, the purple curve illustrates the path of the gas stream, and the central plus sign shows the location of the center of mass of the binary. The outer blue plus signs mark the Richards HET data, while the circles are KPNO data: blue is from Richards and red/purple are the first/second Peters runs. The  $H\alpha$  spectra provide dense coverage of the entire orbital cycle.

(A color version of this figure is available in the online journal.)

We also analyzed 43 UV spectra of AU Mon that were collected with the *International Ultraviolet Explorer (IUE)* on various dates over 16 years from 1978 to 1994. Only the short-wavelength high-resolution *IUE* spectra are considered here; these observations include the most useful diagnostic lines (Si IV, Si II, Al III, etc.) and are of sufficient resolution to permit a detailed comparison with the *Shellspec* models. The IUE Short-Wavelength Prime (SWP) camera covers a range from 1150–1900  $\text{\AA}$  with a resolution of  $\sim 10,000$ . These data have been previously presented, analyzed, and discussed by Peters & Polidan (1982, 1984) and Peters (1994). In this paper, we extend the earlier work by utilizing these UV spectra along with *Shellspec* modeling to ascertain and confirm the parameters for the accretion disk and gas stream of AU Mon.

The binary photometric phase  $\phi_0$  for each observation was calculated with the ephemeris given by Desmet et al. (2010), except that the  $\text{HJD}_{\text{min}}$  given in their Equation (2) has been modified by subtracting 1030 periods so that all the epochs are positive (the effective  $\text{HJD}_{\text{min}}$  then nearly matches that given in Table 2 of Richards & Albright 1999). Figure 1 shows the dense phase coverage obtained of AU Mon at both optical and UV wavelengths. The long-period phase  $\phi_L$  for each observation was calculated from Equation (3) of Desmet et al. (2010). While we label specific observations as *epoch.phase*, we discuss general properties using  $0 \leq \phi < 1$  notation throughout. Some basic properties of the optical and UV data are given in Tables 1 and 2, respectively.

The optical  $H\alpha$  spectra are shown in Figure 2. The phase-dependent properties of the  $H\alpha$  line profile are illustrated (Figure 3) in a “REBECA” diagram (Red Emission, Blue Emission, Central Absorption; see also Budaj et al. 2005 and Miller et al. 2007 for discussion) showing the maximum normalized flux in each emission wing (red and blue triangles) and the deepest point of absorption (green squares). AU Mon shows many of the general characteristics also apparent in TT Hya (above references), including partial disk eclipses near

**Table 2**  
UV Observations

HJD	$\phi_L$	$\phi_0$	Si IV EW ( $\text{\AA}$ )		Si II EW ( $\text{\AA}$ )		Al III EW ( $\text{\AA}$ )		Al III $v$ ( $\text{km s}^{-1}$ ) <sup>a</sup>	
			$\lambda 1394$	$\lambda 1403$	$\lambda 1264$	$\lambda 1309$	$\lambda 1855$	$\lambda 1863$	$\lambda 1855$	$\lambda 1863$
2443873.902	1.87	96.50	1.43	1.08	0.50	0.39	1.14	0.85	-20.5	5.6
2443875.497	1.87	96.64	1.49	1.19	0.83	0.45	1.51	1.19	8.0	25.9
2444484.907	3.36	151.48	1.12	0.92	0.93	0.72	1.34	1.15	25.6	31.1
2444510.971	3.42	153.83	1.30	0.94	0.91	0.65	1.04	0.93	83.8	92.3
2444612.260	3.67	162.94	1.07	0.88	0.94	0.73	1.27	1.16	46.3	57.1
2444616.365	3.68	163.31	0.81	0.59	1.25	0.65	1.04	0.79	9.7	8.5
2445800.515	6.56	269.86	1.52	1.14	1.48	0.84	1.20	1.14	61.7	71.0
2445977.926	6.99	285.83	1.61	1.26	0.81	0.57	1.41	1.23	42.1	79.1
2445982.788	7.00	286.27	1.14	0.98	0.94	0.49	1.13	0.82	-72.3	-35.6
2447422.844	10.51	415.85	1.11	0.81	1.25	0.94	1.06	1.01	91.0	98.3
2447427.074	10.52	416.23	0.87	0.60	0.86	0.65	0.83	0.82	-9.6	0.9
2447550.515	10.82	427.34	1.07	0.79	0.93	0.67	1.25	1.06	15.1	24.2
2447556.534	10.83	427.88	1.24	0.96	0.96	0.63	1.14	1.00	57.3	67.0
2447867.624	11.59	455.87	0.93	0.74	1.35	0.85	1.01	0.94	74.5	82.5
2447789.852	11.40	448.87	1.31	1.12	1.02	0.61	1.19	1.14	107.2	133.1
2447794.882	11.41	449.33	0.82	0.76	0.75	0.55	0.95	0.90	2.7	7.8
2447871.795	11.60	456.25	0.97	0.75	1.14	0.63	0.96	0.92	19.3	25.8
2447938.370	11.76	462.24	1.10	0.73	1.33	0.69	0.87	0.79	-27.4	-15.2
2447945.359	11.78	462.87	1.44	0.80	1.24	0.81	1.10	1.05	62.8	60.6
2448001.258	11.91	467.90	1.27	1.03	0.78	0.41	0.90	0.94	67.7	67.7
2448004.453	11.92	468.18	1.31	0.76	0.91	0.58	0.87	0.88	16.6	21.4
2448228.619	12.47	488.36	0.90	0.73	0.92	0.62	0.92	0.93	27.8	24.8
2448229.691	12.47	488.45	1.05	0.87	0.82	0.62	1.10	1.05	14.7	36.5
2448230.606	12.47	488.53	1.29	0.92	1.17	0.53	1.30	1.14	26.5	29.9
2448231.610	12.47	488.63	1.56	1.24	1.03	0.63	1.49	1.34	30.5	38.2
2448234.611	12.48	488.90	1.75	1.21	1.31	0.65	1.39	1.24	52.4	76.4
2448349.469	12.76	499.23	1.00	0.64	0.99	0.65	0.79	0.81	3.1	1.2
2448351.472	12.77	499.41	0.94	0.70	1.07	0.72	1.00	0.93	12.5	2.9
2448352.460	12.77	499.50	1.00	0.77	1.18	0.77	0.96	0.98	15.4	18.0
2448353.509	12.77	499.59	0.99	0.84	1.05	0.76	1.16	1.06	37.5	39.2
2448356.468	12.78	499.86	1.19	0.86	1.83	1.03	1.25	1.22	59.1	60.6
2448912.776	14.13	549.92	1.76	1.33	1.27	0.42	1.35	1.26	96.0	122.6
2448915.998	14.14	550.21	1.41	0.94	0.79	0.48	0.86	0.94	-29.7	-32.0
2449335.627	15.16	587.97	1.21	1.13	0.84	0.61	1.34	1.31	99.9	126.3
2449375.399	15.26	591.55	2.07	1.04	0.79	0.42	1.54	1.17	-33.1	2.9
2449379.416	15.27	591.91	1.68	1.37	1.04	0.49	1.50	1.54	89.0	113.0
2449383.412	15.28	592.27	1.93	1.31	0.85	0.50	0.75	0.77	-68.4	-76.6
2449658.929	15.95	617.06	1.35	0.97	0.92	0.60	1.06	0.87	12.7	21.0
2449690.597	16.02	619.91	1.29	1.06	0.86	0.50	1.10	1.05	27.9	36.9
2449691.321	16.03	619.98	1.22	0.74	1.04	0.57	0.95	1.04	37.8	57.4
2449691.787	16.03	620.02	1.78	1.37	0.93	0.58	1.20	1.26	8.9	31.5
2449694.603	16.03	620.27	1.12	0.73	0.95	0.50	0.81	0.82	13.0	19.8
2449696.789	16.04	620.47	1.72	1.37	0.97	0.46	1.54	1.37	-5.5	-0.5

**Notes.** The long-period phase  $\phi_L$  and the binary photometric phase  $\phi_0$  are calculated as in Table 1.

<sup>a</sup> The velocity is calculated from the absorption-weighted line center.

primary eclipse and enhanced central absorption near primary eclipse and to a lesser degree near secondary eclipse. However, there is significantly more scatter in the REBECA diagram of AU Mon, particularly in the central absorption. This scatter makes it difficult to ascertain whether additional effects seen in TT Hya are also present in AU Mon; for example, it appears that the tendency for greater blue emission at  $\phi_0 = 0.4\text{--}0.5$  and greater red emission at  $\phi_0 = 0.5\text{--}0.6$  (thought to arise from absorption of the light from the secondary by one side of the disk as well as by the primary; above references) is suggested but not required by these data. The scatter in the central absorption is reduced when the spectra obtained over different regions of the long-period phase are considered separately, and those taken within  $0.35 < \phi_L < 0.85$  show deeper central absorption than those taken within  $\phi_L > 0.85$  or  $\phi_L < 0.35$ . Similar tendencies have been identified by Barría & Mennickent (2011).

The UV line profiles also show phase-dependent variation, as illustrated in Figure 4. The fractional change in equivalent width is calculated for each observation as  $(EW - EW_{\text{med}})/EW_{\text{med}}$ , where  $EW_{\text{med}}$  is the median equivalent width, and the velocity is calculated from the offset of the absorption-weighted line center from the lab wavelength for that transition. The relative absorption strength of Si IV versus Si II shows a striking dependence on the long-period phase, which reflects changes in the disk absorption, gas stream variability, and overall heating of the photosphere (Peters 1994). The long-term variation in Si II is primarily due to changes in disk absorption that maximizes around a  $\phi_L$  of 0.5–0.8. The Si IV variations are predominantly on the trailing hemisphere and reflect an enhancement of the HTAR (Peters & Polidan 1984) and some Si IV absorption from the gas stream. The correlation with  $\phi_L$  of H $\alpha$  central absorption, Si IV and other HTAR lines versus Si II equivalent

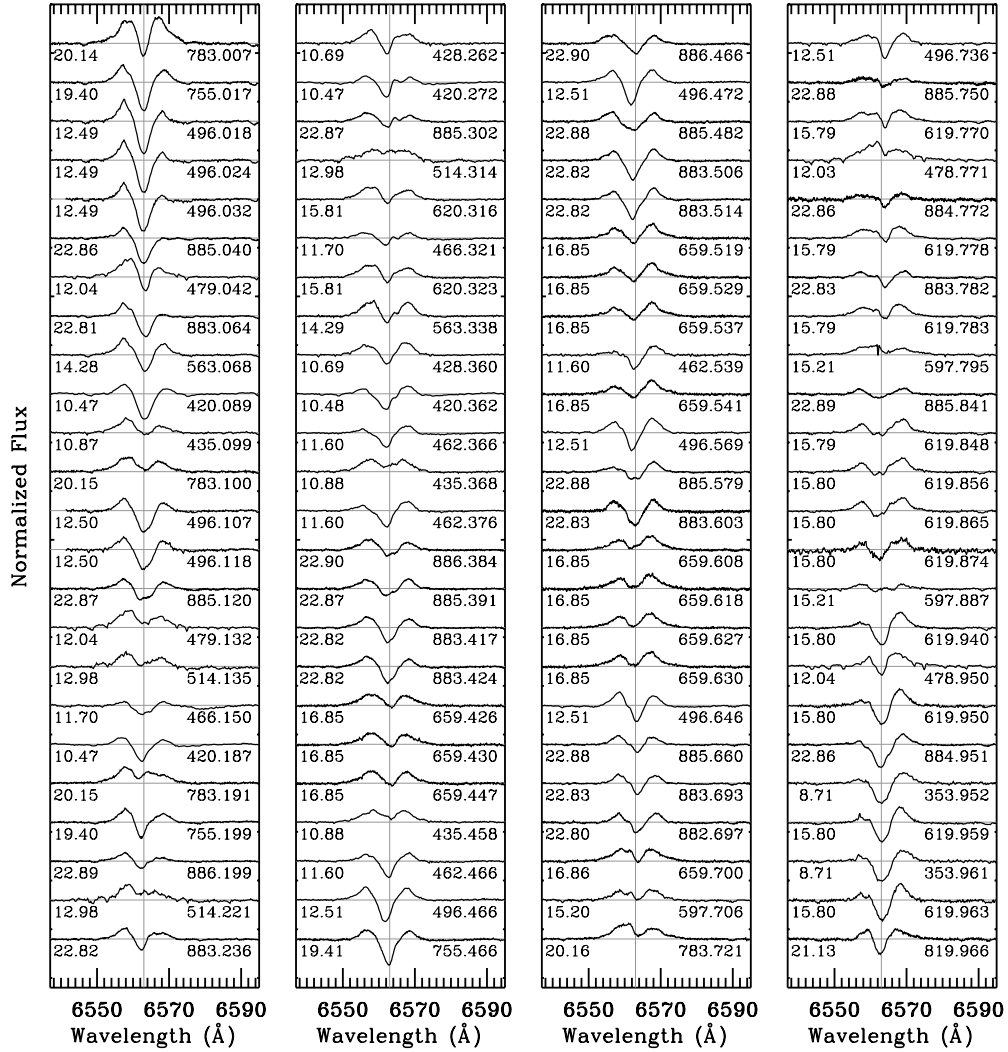


**Figure 2.** Normalized H $\alpha$  spectra of AU Mon. The long-period phase  $\phi_L$  and the binary photometric phase  $\phi_0$  are indicated at left and right, respectively, with the epoch also provided prior to the decimal. The spectra are shown in order of increasing  $\phi_0$ . The HET/HRS data span  $\phi_0 = 882\text{--}886$ .

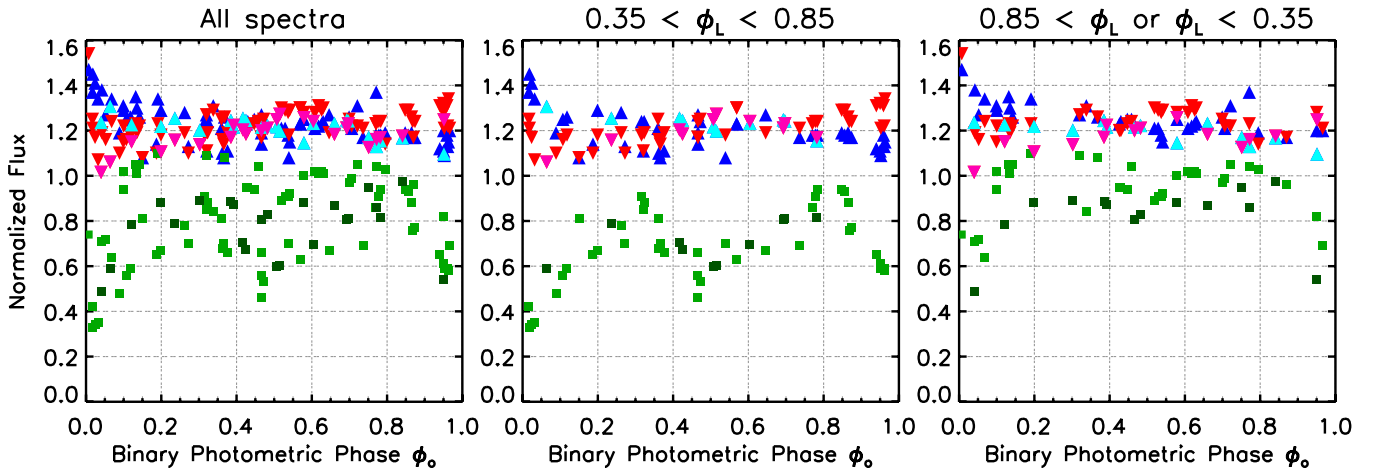


**Figure 3.** REBECA diagram showing the red emission (red triangles), blue emission (blue triangles), and central absorption (green squares) for AU Mon vs. the binary photometric phase  $\phi_0$ . The data points indicate the maximum normalized flux for the emission wings and the deepest point for the central absorption. The HET/HRS data are distinguished with slightly modified colors (pink/cyan/dark green). When the data are separated by long-period phase, it is apparent that the central absorption is deeper for  $0.35 < \phi_L < 0.85$ .

(A color version of this figure is available in the online journal.)

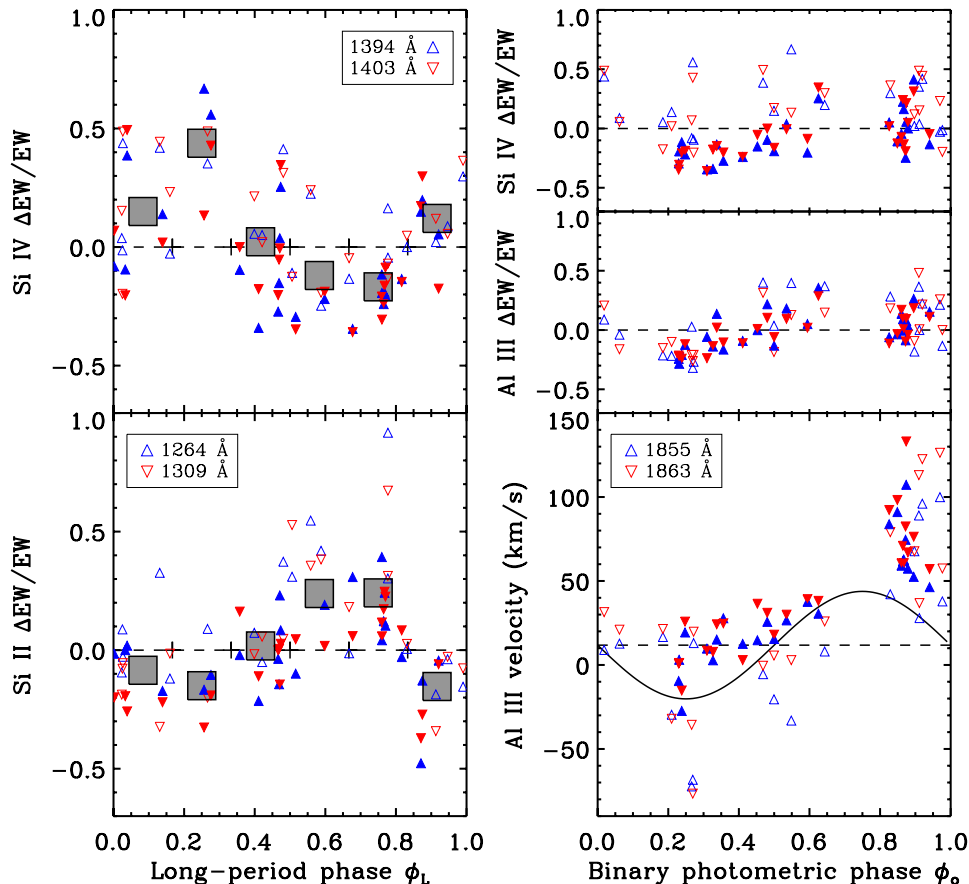


**Figure 4.** Properties of the UV absorption features in AU Mon plotted vs. long-period phase  $\phi_L$  (left column) and binary photometric phase  $\phi_0$  (right column). The filled points in the left-hand column are for  $0.1 < \phi_0 < 0.8$  (i.e., outside of primary eclipse and outside of the absorption influence of the gas stream), and the filled points in the right-hand column are for  $0.35 < \phi_L < 0.85$ . The fractional change in equivalent width  $\Delta EW/EW$  is calculated for each point as  $(EW - EW_{\text{med}})/EW_{\text{med}}$ , where  $EW_{\text{med}}$  is the median equivalent width. The gray squares are means of all points within that sixth of the phase cycle (bounds indicated on the central dashed line). Velocities are for the absorption-weighted line center.

(A color version of this figure is available in the online journal.)

widths and the UV flux distribution do not support ascribing the long-term brightness variation to attenuation by circumbinary material (Desmet et al. 2010; Djurašević et al. 2010). Instead, these periodic tendencies are consistent with the hypothesis of variable mass transfer over the long-period phase (e.g., due to oscillations in the size of the secondary), peaking near  $\phi_L \sim 0.4$ , with the consequent build up of a thick disk over  $\phi_L = 0.5\text{--}0.8$  (Peters 1994; the long-period phases in that paper should be adjusted by about  $-0.1$  to match the ephemeris of Desmet et al. 2010). The circumpolar envelope conjectured by Barría & Mennickent (2011) is a similar concept. A thick disk, enduring over 10–20 orbital periods, can produce both the enhanced Si II absorption and the deeper H $\alpha$  central absorption seen during  $0.35 < \phi_L < 0.85$ , and typically decrease the light from the primary through continuous and line opacities. The collapse of the thick disk could then heat the photosphere of the B star and perhaps generate the 10,000–14,000 K plasma suggested by Peters (1994) as the well-tuned system recovers to equilibrium before the next episode of enhanced mass transfer. In this scenario, the self-similar orbital light curve shape at long-period maxima and minima (Desmet et al. 2010; Djurašević et al. 2010) may indicate that as the thick disk collapses the outer regions puff up or flare to extend beyond the orbital plane, which is potentially related to the L3 mass loss near maximum long-period brightness proposed by Peters (1994).

Some of the UV line profiles also vary with the binary photometric phase  $\phi_0$ . For example, the Al III doublet shows increased redshifted absorption near the binary photometric phase of  $\phi_0 \sim 0.85$ , ascribed by Peters (1994) to absorption within the infalling gas stream. In Section 3.2, we demonstrate through *Shellspec* modeling that this effect can indeed be produced by the gas stream.

### 3. SHELLSPEC MODELING

The system parameters used to create the synthetic spectra were primarily taken from the mean *CoRoT* disk model of Djurašević et al. (2010, their Table 1). In particular, we adopt their system inclination of 80.1 deg, component separation of  $42.1 R_\odot$ , primary mass of  $7.0 M_\odot$ , mass ratio of  $q = 0.17$ , and primary radius of  $5.1 R_\odot$ ; the secondary dimensions are specified by the Roche surface calculated within *Shellspec* (Budaj & Richards 2004). We briefly investigated alternative values of inclination and primary radius in our modeling and confirmed that the Djurašević et al. (2010) values gave optimal results. The primary and secondary velocities are set to 30.9 and 161 km s $^{-1}$ , respectively, which are deprojected from the measured  $K$  values given in Desmet et al. (2010, their Table 6). The system parameters are fixed throughout the process of modeling the accretion disk and gas stream.

**Table 3**  
Shellspec Model Parameters

Parameter	Primary	Secondary	Accretion Disk	Gas Stream
Temperature (K)	17000	5750	14000 <sup>a</sup>	8000
Radius <sup>b</sup> ( $R_{\odot}$ )	5.1	10.1	5.1, 23	4.0
Disk thickness ( $R_{\odot}$ )	...	...	5.2	...
Mass ( $M_{\odot}$ )	7.0	1.2	...	...
Density ( $10^{-15}$ g cm $^{-3}$ )	...	...	100	60
$v_{\text{rot}}$ (km s $^{-1}$ )	118.3	44.7	...	...
$v_{\text{turb}}$ (km s $^{-1}$ )	...	...	30	100
$v_{\text{orb}}$ (km s $^{-1}$ )	-30.9	161	-30.9	...
$v_{\text{init}}, v_{\text{final}}$ (km s $^{-1}$ )	...	...	...	100, 500

**Notes.** The modeling process and the estimated uncertainties are detailed in Section 3.

<sup>a</sup> The temperature of the accretion disk is a function of radius; the given value is the maximum temperature.

<sup>b</sup> The radius of the secondary is the average Roche lobe radius. The inner and outer disk radii are given. The separation between the primary and secondary is  $42.1 R_{\odot}$ .

The general method used to produce and evaluate *Shellspec* models was as follows. First, synthetic stellar spectra were generated for the primary and secondary stars, using the program SPECTRUM (Gray & Corbally 1994). SPECTRUM was run with model stellar atmospheres produced by Castelli & Kurucz (2003) with ATLAS9. The effective temperature and surface gravity for the primary were identified through comparison to synthetic spectra with particular attention paid to the UV lines; we find that a B3 stellar type with  $T \simeq 17,000$  K and  $\log g \simeq 3.5$  provides a good match. Note that this temperature is more consistent with the primary mass found by Desmet et al. (2010), whereas they note that their preferred value is somewhat lower than is typical for this spectral class. For the secondary, we assume  $T = 5750$  K and  $\log g = 2.5$ , as found by Desmet et al. (2010). The resulting synthetic stellar spectra were used as input for *Shellspec*, which was then run to create synthetic composite spectra for the system at phases matching our observational coverage. The parameters specifying the primary and secondary star, given in Table 3, were held fixed throughout the modeling process and can be compared with the separation between the primary and secondary, which is  $42.1 R_{\odot}$ . The shape of the secondary star is calculated by *Shellspec* assuming that it fills its Roche lobe, hence the quoted radius is the average Roche lobe radius. The parameters specifying the accretion disk were set interactively for each trial; Table 3 lists those from our final preferred model. A gas stream (with parameters held constant) was also included for most of the modeling, as described below. Finally, the output synthetic composite spectra were compared to the observed spectra at a range of phases. As part of this process, difference profiles were computed by subtracting the synthetic from the observed spectra.

We identified through trial and error an initial set of accretion disk parameters that provided a reasonable match to the observed optical and UV spectra, then considered the effect of the mass-transfer stream before further refining the disk model. The influence of the gas stream is subtle relative to that of the disk, and the precise properties of the stream are only loosely constrained here. After examining a range of parameters, we adopted a set that successfully reproduces the redshifted absorption observed in Al III (and to a lesser degree in H $\alpha$ ) at  $0.75 < \phi_0 < 1.0$ . This stream component was then included unchanged in all subsequent modeling, while the disk param-

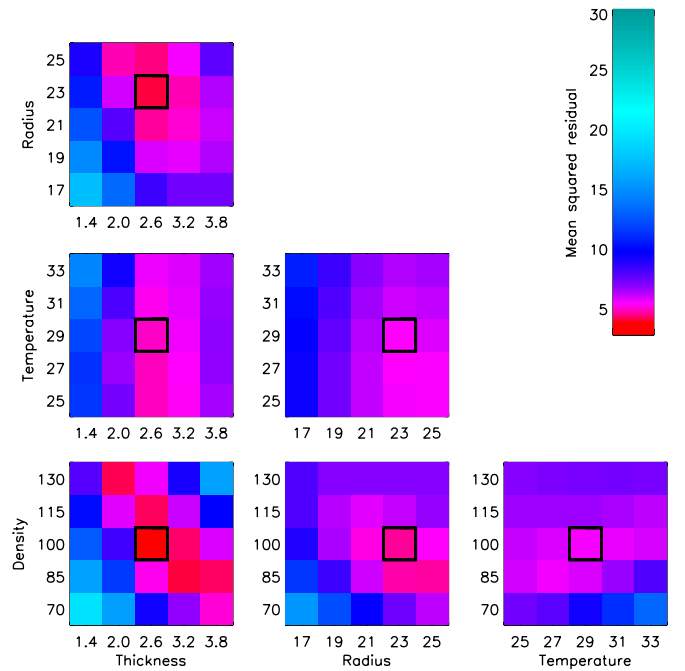


**Figure 5.** Accretion disk modeling, evaluated against HET H $\alpha$  spectra taken at a representative set of nine phases. The accretion disk parameters varied are the disk half-thickness, the outer disk radius, the effective temperature, and the density; each parameter is stepped through five values for a total of 625 considered models. The gas stream is included in the modeling with fixed parameters. Models are compared using a goodness-of-fit measure (summed squared residuals), which is shown color-coded (key on right) for projections, by mean, onto parameter subgrids. The overall preferred model is indicated by the bold-bordered squares.

(A color version of this figure is available in the online journal.)

eters were varied over a grid to improve the disk model; consistent inclusion of the relatively minor contribution of the gas stream throughout reduces the possibility of biasing the disk properties by attempting to match an incomplete model to the observations. Additional iterations (e.g., testing a grid of stream models around the best disk model) did not provide additional information.

### 3.1. The Accretion Disk

The free parameters of interest for the accretion disk are the thickness, the outer radius, the characteristic temperature, and the density. The inner disk radius is fixed to be slightly larger than the radius of the primary star, at  $5.2 R_{\odot}$ . The temperature of the disk is a function of radius as given by Equation (58) of Budaj & Richards (2004); e.g., for a characteristic temperature of 27,000 K, the disk temperature increases to a maximum value of  $\simeq 13,200$  K at a radius of  $9 R_{\odot}$  and then decreases to a temperature of  $\simeq 9500$  K at  $20 R_{\odot}$ . The density of the disk is set to scale inversely with radius, with the initial density specified at the inner radius of the disk.

A total of 625 potential models were generated by varying these four parameters through five different values each, straddling the parameters of the initial model used to characterize the stream. Specifically, the considered values spanned  $2.8\text{--}7.6 R_{\odot}$  in steps of  $1.2 R_{\odot}$  for thickness;  $17\text{--}25 R_{\odot}$  in steps of  $2 R_{\odot}$  for outer radius;  $25,000\text{--}33,000$  K in steps of 2000 K for characteristic temperature; and  $(70\text{--}130) \times 10^{-15}$  g cm $^{-3}$  in steps of  $15 \times 10^{-15}$  g cm $^{-3}$  for density. The degree to which each model matched the data was assessed through calculation of a goodness-of-fit statistic (sum of squared residuals within

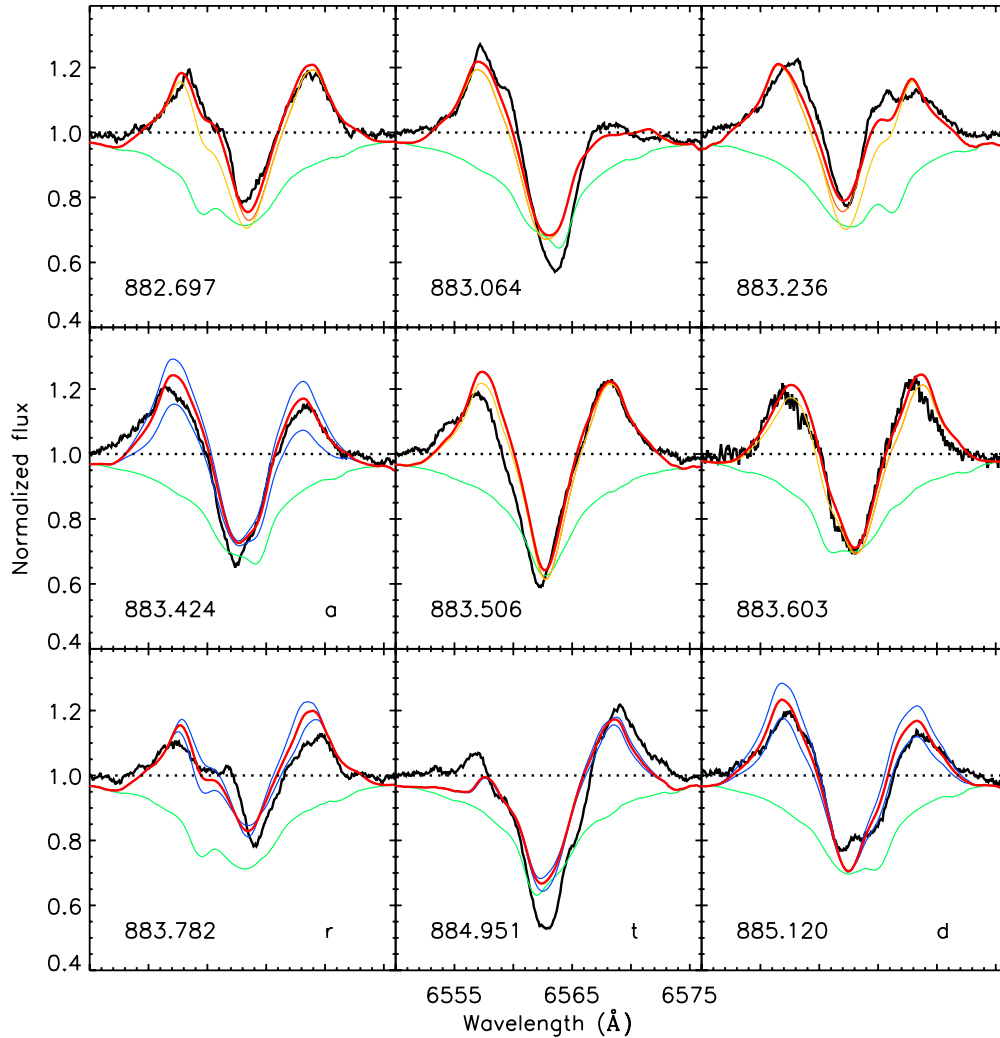


**Figure 6.** Preferred model for the accretion disk+stream+spot is plotted (red) along with the HET  $H\alpha$  profiles (black) at the nine considered representative phases; the stars-only model is shown in green for reference. The four frames at the bottom and middle left show (in blue) the results of changing the disk half-thickness, outer radius, effective temperature, and density by  $\pm 1$  step along the grid displayed in Figure 5. The five frames at the top and middle right show the stars+disk and stars+disk+stream models in yellow and orange, respectively.

(A color version of this figure is available in the online journal.)

the relevant spectral region), determined for each model at each of the 24 HET phases for  $H\alpha$  and  $H\beta$  and at each of the 47 *IUE* phases for Al III and Si IV. The other  $H\alpha$  data were not considered in this process, since it is desirable to model the  $H\alpha$  emission over a sufficiently short time interval to exclude long-term dynamical changes that might occur in the accretion disk.

The results of the modeling are shown in Figure 5 for a representative set of nine HET/ $H\alpha$  phases covering the full orbit. The agreement with the fit is illustrated using a color scale (red indicates good agreement, blue a poor match) for parameter pairs; the goodness-of-fit indicator is projected across the other two parameters using mean values. Each cell is therefore constructed from nine phases and projected down from 25 models. While there is some unavoidable degeneracy in the  $H\alpha$  modeling (e.g., increased disk emission may be obtained either from increasing the density or the thickness), there are clearly favored regions of parameter space. Specific consideration of the eclipse phases is helpful for clarifying the structure, and the goodness-of-fit for Al III and Si IV across identical grids provides useful additional constraints upon temperature. It appears that

models at the extreme ends of the grid are excluded; for example, there is only poor agreement with observations for models with simultaneously large values of thickness and outer radius, or thickness and density, or outer radius and density, and similarly poor agreement for simultaneously small values of those parameters. The disk is most readily apparent in the double-peaked  $H\alpha$  emission, and hence the HET/ $H\alpha$  data drive the modeling. However, the disk is also visible in the difference profiles for other optical (e.g.,  $H\beta$ ; Figure 7) and UV lines, and the additional spectral constraints help lift degeneracies in the disk parameters that are present if analysis is restricted to the  $H\alpha$  line.

From the *Shellspec* modeling, we derived preferred parameters for the accretion disk (marked on Figure 5 by bold-bordered squares; see also Table 3): a thickness of  $5.2 R_{\odot}$ , an outer radius of  $23 R_{\odot}$ , a characteristic temperature of 29,000 K (corresponding to a maximum temperature of  $\simeq 14,000$  K), and a density of  $100 \times 10^{-15} \text{ g cm}^{-3}$ , with a turbulence velocity of  $30 \text{ km s}^{-1}$ . Some of the other disk models considered cannot be ruled out; for example, with higher densities ( $130 \times 10^{-15} \text{ g cm}^{-3}$ ) a smaller thickness ( $4.0 R_{\odot}$ ) is possible, or alternatively with

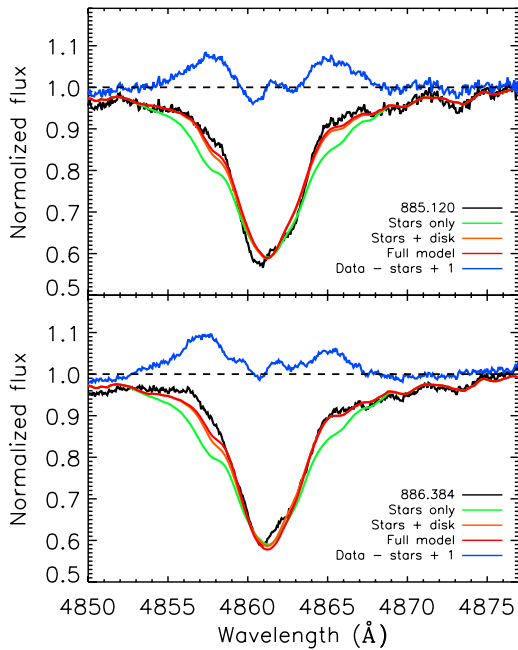


**Figure 7.** Model for the  $H\beta$  line compared to HET spectra (black) at  $\phi_0 = 0.120$  (top) and  $\phi_0 = 0.384$  (bottom). The model with only stars (green) has deeper absorption wings than are observed. Adding an accretion disk (orange; see Section 3.1) significantly improves the match, and the full model (red) provides reasonable agreement to the data. The difference profile (blue) shows the underlying double-peaked emission signature of the disk, similar to what is seen directly in the observed  $H\alpha$  profile. The synthetic stellar spectrum for the primary was calculated with  $\log g = 3.0$  only in the case of  $H\beta$  to provide a better match with the observed profile.

(A color version of this figure is available in the online journal.)

lower densities ( $85 \times 10^{-15} \text{ g cm}^{-3}$ ) a larger thickness ( $6.4 R_\odot$ ) is possible. A larger outer disk radius is tenable, and in general models bordering the preferred parameters acceptably match the data.

By examining the  $H\alpha$  profiles (e.g., Figure 6), we found that the preferred disk plus stream model gives a slightly improved match to observations with the additional inclusion of a relatively minor “spot” component. This spot is located at the outer disk edge at coordinates of  $(-18, -18) R_\odot$  (in a primary-centered system) with a radius of  $2.6 R_\odot$ , a temperature of 8000 K, a density of  $80 \times 10^{-15} \text{ g cm}^{-3}$ , a velocity vector of  $(-120, 120) \text{ km s}^{-1}$ , and a turbulence of  $100 \text{ km s}^{-1}$ . These parameters have large uncertainties of  $\sim 30\%$ – $40\%$ , since this spot has only an incremental impact on the model profile. This “spot” may be physically associated with disk asymmetries, such as caused by an elliptical rather than circular shape, a clumpy structure, or brighter regions. One example is the high-density LR along the line of centers between the stars where the gas that has circled the primary slows down because of contact with the incoming gas stream (Richards 1992).

The preferred model (including stars, disk, stream, and spot) is plotted in Figure 6 along with the same representative set of nine HET/ $H\alpha$  spectra used to generate Figure 5. In the lower left subplots, the effect of varying one parameter in isolation by one step along the grid is shown. Our estimated uncertainties on the modeled accretion disk parameters are one grid step; for example, the outer radius is  $23 \pm 2 R_\odot$ . In the upper right subplots, the models for the disk alone and for the disk plus stream are also shown. In the model, it is clear that a substantial fraction of the  $H\alpha$  emission originates from the disk. During the partial primary eclipse, only a small fraction of the central disk

region is eclipsed, which may slightly reduce the  $H\alpha$  emission. However, since the contribution to the spectral continuum due to the primary star (the dominant source of light in the system) is significantly diminished at these phases, the  $H\alpha$  emission is strongly enhanced relative to that continuum. This result occurs because the spectra are not displayed in absolute units but are normalized relative to the continuum. This effect is naturally taken into account in *Shellspec*.

Our modeling suggests that the accretion disk extends to larger radii and is thicker than found by Djurašević et al. (2010) from their analysis of *CoRoT* and *V*-band light curve data. However, our *Shellspec* calculations are primarily based on  $H\alpha$  spectroscopy for which the disk is visible in emission even when the line is optically thin; in contrast, the disk as modeled by Djurašević et al. (2010) is non-transparent (optically thick in the continuum), which results in smaller dimensions. In addition, their disk includes a hot spot and two bright spots, which produce embedded compact regions of enhanced emission, while our disk is circularly symmetric. Consequently, the differences in disk dimensions are not necessarily in conflict. Indeed, our disk may be regarded as having a wavelength-dependent effective size, which is a function of the opacities in the lines and in the continuum. It is additionally possible that the parameters of the disk when modeled by Djurašević et al. (2010) physically differed from those present when we collected our HET observations, which serve as the primary basis for our modeling. The large disk in AU Mon may explain the particularly prominent  $H\alpha$  emission that is visible near primary eclipse; this is different from V393 Sco, for which the disk is likely to be more optically thick and less extended (Mennickent et al. 2012).

### 3.2. The Gas Stream

The free parameters of interest for the gas stream are the initial and final velocities, the initial density, the temperature, the radius, and the turbulence. In the *Shellspec* code, the density within the stream decreases as the material falls toward the primary star, such that  $v\rho$  remains constant along the length of the stream. The coordinates of the origin and termination of the stream are specified within the code, and form the endpoints of the straight cylinder that represents the stream. In this case, the stream extends from  $(35, 0) R_\odot$  to  $(5, 5) R_\odot$ . Similar results are expected from a finer geometric model of the stream that takes into account its curvature due to orbital motion, the full velocity field, and likely changing radius. The preferred parameters for the stream are initial/final velocities of  $100/500 \text{ km s}^{-1}$ , an initial density of  $6 \times 10^{-14} \text{ g cm}^{-3}$ , a temperature of 8000 K, a radius of  $4 R_\odot$ , and a turbulent velocity of  $100 \text{ km s}^{-1}$ ; with relatively large uncertainties of  $\sim 15\%$ – $25\%$ .

The influence of the gas stream is apparent as absorption at  $0.75 < \phi_0 < 1.0$ , as discussed in Section 2. For example, inclusion of the stream has no appreciable impact on the modeled Al III line profile at low orbital phases, but Figure 8 illustrates that at  $\phi_0 = 0.878$  the infalling stream, viewed here against the primary, generates significant redshifted absorption that improves the agreement between model and observations. We noticed that the blue side of the Al III lines was variable near orbital phase 0.5; this is similar to the Si II variability observed by Peters (1994) which was interpreted as due to episodic mass loss. The final model provides a reasonable match to this variable Al III line profile. The absorption at high orbital phases is less noticeable at  $H\alpha$  since a mass transfer stream will tend to absorb relatively more light at shorter wavelengths (e.g., Olson & Bell

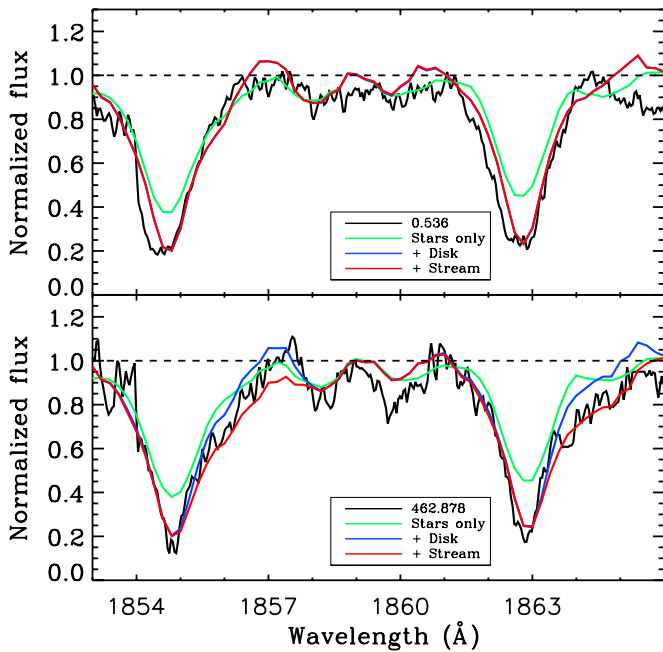


**Figure 8.** Models for Al III compared to *IUE* data (black) at  $\phi_0 = 0.536, 0.878$ . The model with only stars (green) has shallower central absorption than the data. Adding an accretion disk (blue; see Section 3.1) is a good match at  $\phi_0 = 0.536$  but overpredicts the red-wing emission at  $\phi_0 = 0.878$ ; here, better agreement is obtained when the gas stream (red; see Section 3.2) is also incorporated. The observed spectrum in the top frame is the average from phases  $\phi_0 = 499.511$  and  $591.560$ .

(A color version of this figure is available in the online journal.)

1989). However, at a temperature of 8000 K the stream also acts to provide additional  $H\alpha$  emission at other phases; for example, at  $\phi_0 = 0.697$  the stream generates slightly blueshifted emission that improves the agreement between model and observations (Figure 6). Inclusion of the stream has only a negligible effect for the  $H\beta$  (Figure 7) and Si IV regions.

The velocity and density adopted for the gas stream correspond to a mass transfer rate of  $\sim 2.4 \times 10^{-9} M_{\odot} \text{ yr}^{-1}$ ; this should be regarded as a lower limit since the loosely constrained temperature of the stream is set near the peak emissivity of  $H\alpha$ . Measurements of any changes in the period over the last several decades would provide an independent estimate of the mass transfer rate in AU Mon. The rate we derive here from *Shellspec* modeling is broadly similar to mass transfer estimates for other long-period Algol-type binary systems, such as TT Hya ( $P = 6.95$  days,  $q = 0.27$ ), for which Miller et al. (2007) calculated a rate of  $\geq 2 \times 10^{-10} M_{\odot} \text{ yr}^{-1}$ , or the non-eclipsing CX Dra ( $P = 6.70$  days,  $q = 0.23$ ), for which Simon (1998) calculated a rate of  $10^{-10}$  to  $10^{-8} M_{\odot} \text{ yr}^{-1}$ .

## 4. SPECTRAL VARIABILITY

### 4.1. $H\alpha$ Variability

The  $H\alpha$  spectra described in this work reveal changes in the emission line profile on both short (multi-week) and long (multi-year) timescales over the 20 year period from 1991 to 2011 and covering 697 orbital cycles (see Figure 9); this is consistent with previous observations (e.g., Plavec & Polidan 1976; Sahade et al. 1997; Desmet et al. 2010). The HET data were taken over  $\sim 42$  days ( $\sim 3.8$  orbital periods), with a 10 day gap in the coverage. The 10 spectra obtained prior to this gap typically show deeper central absorption than the 14 spectra

obtained after the gap. This is likely simply due to random short-term variability, although it is alternatively possible that the decrease in central absorption depth is partially related to the modest increase in the long-period phase, which transitions from  $\phi_L \leq 22.83$  to  $\phi_L \geq 22.86$  over the gap in coverage. Figure 9 illustrates the rapidity with which the profile can change over only two orbital cycles (e.g., epoch 883 to 885).

We ran the grid of models on five subsets of  $H\alpha$  spectra, separated by long-period phase, to investigate potential changes in the structure of the disk. The subsets were grouped as  $12.49 \leq \phi_L \leq 12.51$  (Peters KPNO),  $15.79 \leq \phi_L \leq 15.81$  (first Richards KPNO),  $16.85 \leq \phi_L \leq 16.86$  (second Richards KPNO),  $22.80 \leq \phi_L \leq 22.83$  (first HET), and  $22.86 \leq \phi_L \leq 22.90$  (second HET). Although the preferred model is better matched to the first set of HET spectra than to the second, the change in central absorption does not systematically alter the relative goodness-of-fit across the model grid (i.e., generally the same subset of models remains favored). The Peters KPNO spectra are also reasonably well fit by the preferred model and its similar cousins. In contrast, both sets of Richards KPNO spectra have increased emission and are better fit by a stronger disk, for example, with a thickness of  $6.4 R_{\odot}$  and an outer radius of  $25 R_{\odot}$ ; it is additionally necessary to increase the stream contribution through changing the density to  $120 \times 10^{-15} \text{ g cm}^{-3}$ , but this is still not sufficient to provide a very good match to the shallower central absorption.

The excess low-velocity emission suggests the presence of additional material beyond that contained in the circularly symmetric disk and the stream (see tomography results in Section 5); while the disk remains dominant, the residual emission seems more centralized. This behavior is reminiscent of CX Dra, for which Richards et al. (2000) concluded that the emission originates primarily between the stars as a result of the impact of the stream onto the outer edge of an extended disk. It is also consistent with vertical outflows similar to the bipolar wind hypothesized in the DPV V393 Sco (Mennickent et al. 2012). In any event, since the long-period phase is similar for the Richards KPNO and the HET data, these results demonstrate that the long-period phase is not the sole driver of  $H\alpha$  variability.

### 4.2. Transient UV Feature

The model presented in Section 3 including the stars, disk, stream, and a standard spot provides a good match to the majority of the *IUE* observations. However, an additional secondary absorption feature is present in several spectra. This transient spectral feature has the following characteristics: (1) the profile shape appears to require some blueshifted absorption, rather than arising exclusively from a spike of low-velocity emission; (2) the feature is only found in spectra obtained at  $0.84 < \phi_0 < 0.99$ , although most spectra at these phases do not show the feature; (3) there is no obvious correlation in the presence of this feature with the long-period phase  $\phi_L$ ; and (4) the feature is present in 5/13 cases in Si IV and in 2/13 cases also in Al III and Si II. (There is one exceptional case in which the line profile is distorted at Al III but not Si IV, at an intermediate phase, but here the profile may be more consistent with excess low-velocity emission.) This feature is unlikely to be related to any potential calibration issues, since it has a consistent profile when it is present in both Si IV and Al III. It is also unlikely to be of geocoronal or interstellar origin, since it is variable and its presence is confined to a specific system phase.

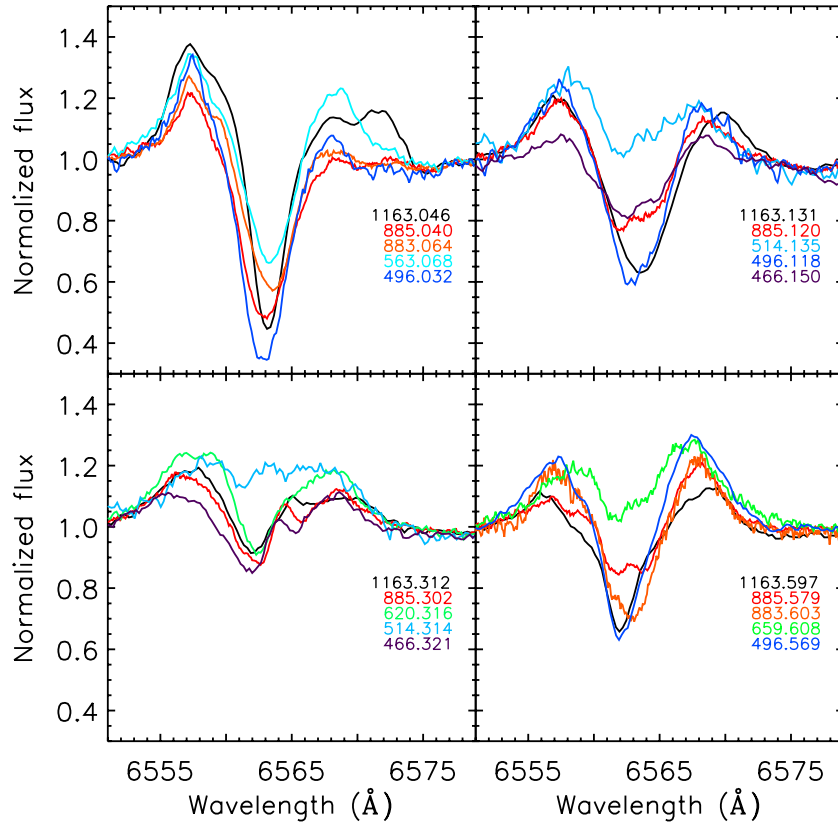


**Figure 9.** Long-term variability in the  $H\alpha$  line profile. The contrast over the 20 year period from 1991 to 2011, over 697 orbital cycles from epoch 466 to 1163, illustrates the extent of the line profile changes in AU Mon. The variation over only two orbital cycles from epoch 883 to 885 demonstrates the rapidity with which the profile can change.

(A color version of this figure is available in the online journal.)

The transient UV feature could in principle result from some combination of blueshifted absorption and increased central emission. For example, Bisikalo & Kononov (2010) discuss a flare in the CV SS Cyg that generated strong  $H\gamma$  emission while also broadening the absorption. Another possibility is that the feature results from a P-Cygni profile overlaying the stellar absorption, although this would require material at larger radii (limiting the temperature and hence the impact on Si IV). In AU Mon, the feature primarily modifies the blue side of the profile, and the absorption then extends to shorter wavelengths than the disk plus stream model predicts. We conjecture that the transient spectral feature is associated with an occasional outflow arising in the vicinity of the disk–stream interaction site, which is hot and of variable temperature. It is possible that such an outflow could be related to the HTAR described by Peters & Polidan (1984, 1998) and that both are consequences of the stream impacting the disk and primary. In this context, the van Rensbergen et al. (2011) result may be relevant: that Algols with hotter primaries (such as AU Mon) may experience more mass loss than those with cooler primaries (such as TT Hya).

We used *Shellspec* to verify that it is possible to produce such an outflow feature (Figure 10) by using a second “spot” component in addition to the spot applied in the full model to represent the LR between the stars; the extra spot is only used here to illustrate the transient UV feature. An “outflow spot” located at coordinates of  $(8, 6) R_{\odot}$  with a velocity vector of  $(120, 120) \text{ km s}^{-1}$  and with a spot radius/density/temperature of  $4 R_{\odot}/30 \times 10^{-15} \text{ g cm}^{-3}/12,000 \text{ K}$ , significantly improves the agreement between the modeled and observed UV spectra for those cases in which this additional absorption feature is present.

The degree of improvement varies, as might be expected given the variable nature of the feature itself. Although the outflow spot parameters are based on the UV spectra, the addition of this component would also improve the agreement between the modeled and observed optical spectra in several cases. For example, both the  $H\alpha$  and  $H\beta$  spectra at  $\phi_0 = 883.236$  show features in the red wing that are better matched when the transient outflow is included; this effect may be partially due to the outflow spot component replacing disk emission within the overlapping region.

## 5. APPLICATION OF DOPPLER TOMOGRAPHY

Doppler tomography provides an independent method of investigating the accretion structure of AU Mon, and of evaluating the accuracy of the *Shellspec* modeling (described in Section 3). The basic assumptions and constraints of Doppler tomography include (Marsh & Horne 1988; Richards 2004): (1) the spectra are assumed to be broadened primarily by Doppler motions, (2) spectra with high wavelength resolution and good resolution in orbital phase (or projections) are needed to create a well-resolved image, (3) spectra dominated by emission lines are primarily used in the analysis, (4) the gas is assumed to be optically thin, and (5) the object (velocity field+state quantities) does not change with time. Several accretion structures have been identified in the 2D and 3D Doppler tomograms based on optical and ultraviolet spectra of Algol-type binaries (e.g., Richards 2004; Richards et al. 2012). These include classical and transient accretion disks, the gas stream, emission from the chromosphere and other magnetic structures on the donor star

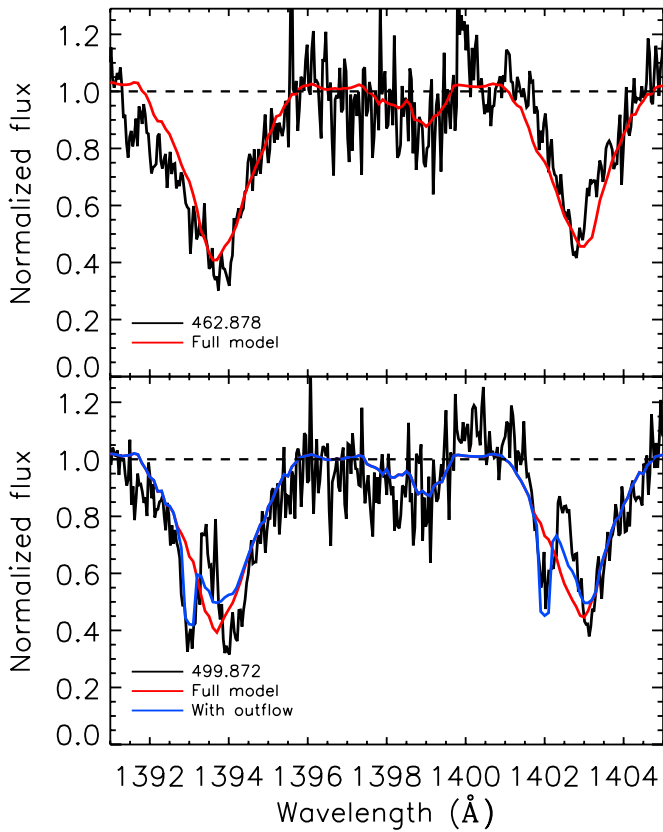


**Figure 10.** Models for Si IV compared to *IUE* data (black) near  $\phi_0 = 0.87$  for epoch 462 (top) and 499 (bottom). A subset of the UV spectra, including at epoch 499 (but not 462), display a secondary blueshifted absorption feature that may indicate a transient outflow. (The Al III profile at 499.872 shows a similar effect.) The standard model (stars, accretion disk, gas stream, and spot/localized region) is shown in red, and a modified model with an added “outflow” spot component is shown in blue. The extended model with the outflow component provides a better match to the observations.

(A color version of this figure is available in the online journal.)

(e.g., prominences and coronal mass ejections), shock regions, an accretion annulus, and an absorption zone (corresponding to a region of hotter gas). Moreover, tomography was used to demonstrate the quality of *Shellspec* models for the gas stream and disk in TT Hya, and to discover that the disk in TT Hya is asymmetric (Miller et al. 2007). This procedure was extended for the study of AU Mon.

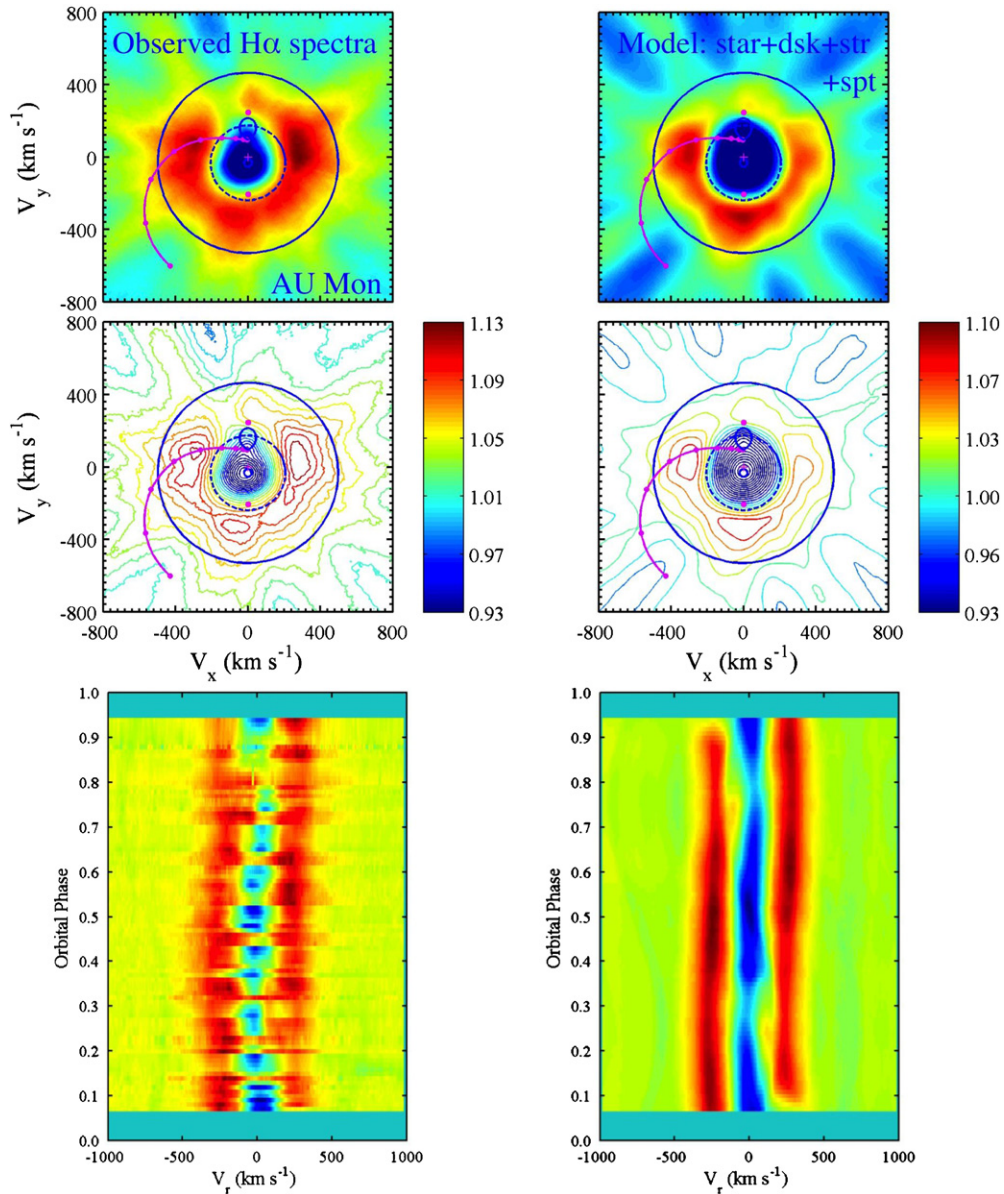
The observed spectra of AU Mon obtained over a range of phases were combined to construct a 2D velocity–space map of the emission from the stars and accretion structures. Figure 11 shows the good match between the observed spectra and the model based on the stars, disk, stream, and a spot/LR. The left frames show the Doppler tomogram, contour map, and interpolated trailed spectrogram based on the observed spectra, while the right frames show the results based on the combined model for the stars, disk, stream, and spot. The observed tomogram shows that the strong H $\alpha$  emission arises primarily from the region in the tomogram that corresponds to the locus of a circular Keplerian accretion disk. Since a non-Keplerian disk would have a range of lower velocities, the tomogram suggests that the disk is Keplerian. The gap in the H $\alpha$  disk emission seen near  $V_x = 0$ ,  $V_y > 0$  is due to limited coverage at those phases (see Figure 1). The contour maps show that the model is fairly close to the observations.

Figure 12 shows the 2D Doppler tomograms obtained when the model spectra for the various structures (stars, disk, stream, and spot) are sequentially removed from the observed spectra. This figure shows the Cartesian representation of the binary (top left), the observed and combined model tomograms (top right), the difference tomograms in sequence (middle frames) for (1) observed-stars, (2) obs-(stars+disk), (3) obs-(stars+disk+stream), and (4) obs-(stars+disk+stream+spot). The images for the latter three are enhanced in the bottom frames. It is apparent that the H $\alpha$  emission in AU Mon is dominated by the accretion disk, then by the stream, and spot (LR). The relatively weak contribution from the gas stream is apparent in the tomogram of the synthetic spectrum constructed from the stars+disk+stream model, and in the tomogram of the difference profile when the stars+disk model is subtracted. The bulk of the stream emission occurs at velocities less than  $\sim 400$  km s $^{-1}$ , corresponding to the relatively-higher density regions closer to the stream launch point at L1. This may reflect the inner stream being subsumed within the disk as it approaches the primary, which is modeled in *Shellspec* through prioritizing the disk in overlapping regions.

The images show that we have successfully modeled the dominant part of the disk, the gas stream, and the brightest part of the LR spot feature. However, the final image shows that there are still two parts of the image that remain: a low-velocity region near the LR and also an asymmetric portion of the disk. The location of this residual emission in velocity space is broadly similar to that observed in TT Hya, which Miller et al. (2007) ascribed to an asymmetric disk, as supported by hydrodynamic simulations by Richards & Ratliff (1998); it seems plausible that the disk in AU Mon is also asymmetric. Moreover, compared to TT Hya, the residual emission in AU Mon is more pronounced and has clearly sub-Keplerian velocities.

A possible explanation for these lower velocities is that the stream in AU Mon makes a nearly tangential collision with the primary (see Figure 1), reducing the circular speed of the continuing flow, which could then contribute additional low-velocity emission, particularly along the line of centers where the density rises due to conservation of particle flux as it collides with the incoming gas stream. In the case of TT Hya, the system geometry precludes the stream from a direct collision with the primary. Given the early spectral type of the primary in AU Mon, it is also possible that the residual emission seen in the tomogram could be explained by a vertical wind or jet as found in  $\beta$  Lyr (Ak et al. 2007) and V393 Sco (Mennickent et al. 2012). The 2D tomograms displayed in Figures 11 and 12 (top frames) suggest that the disk in AU Mon extends almost to the Roche surface of the primary (since the inner disk velocity is similar to that of the Roche surface), so any subsequent gas flow from the L1 point would be intercepted by this extended disk structure and perhaps create a jet-like feature. A similar extended disk structure was also found in CX Dra (Richards et al. 2000). These features might be confirmed later through the application of 3D tomography. In the meantime, it is encouraging that a modified *Shellspec* model with an added outflow spot component beyond the full synthetic spectrum based on the stars+disk+stream+spot/LR can provide a better match to the observations than when the outflow region is excluded; as illustrated in the case of the Si IV line (see Figure 10).

The tomograms do not show any obvious evidence of mass loss or depletion in the emission associated with the L2 and L3 points (see large lavender dots along the line of centers, beyond



**Figure 11.** Comparison between the observed spectra and the model based on the stars, disk, stream, and localized region (labeled “spot”). Left frames show the Doppler tomogram, contour map, and interpolated trailed spectrogram based on the observed spectra, while the right frames show the results based on the combined model for the stars, disk, stream, and spot. The L2 and L3 points are represented by the large lavender dots along the line of centers beyond the secondary and primary, respectively. The contour maps show that the model is fairly close to the observations.

(A color version of this figure is available in the online journal.)

the stars in Figure 12). However, if mass loss has occurred or is in progress, then the tomograms confirm that there is a greater likelihood that the source should be located near the L1 point, as suggested by Barriá & Mennickent (2011).

Although the  $H\alpha$  central absorption changes in depth throughout the long-period cycle (Figure 3), the residual emission revealed in the final frame of Figure 12 is present for both  $0.35 < \phi_L < 0.85$  and  $0.85 < \phi_L < 1.35$ , confirming that this effect is tied to the relative geometry of the stars, disk, and stream, rather than arising from long-period variability such as due to cyclic changes in the mass transfer rate.

## 6. SUMMARY

The main results from our observations and modeling of accretion structures in AU Mon are the following.

1. We confirm that the  $H\alpha$  and UV spectral features display significant variability, some of which is linked to the long-period phase. For example, spectra taken within  $0.35 < \phi_L < 0.85$  show deeper central absorption than those taken within  $\phi_L > 0.85$  or  $\phi_L < 0.35$ . We find that these trends are broadly consistent with the scenario of variable mass transfer proposed by Peters (1994).
2. We use *Shellspec* to self-consistently model the accretion disk and gas stream. Preferred parameters for the disk and stream are determined through comparison with observed spectra; for the accretion disk, they include a thickness of  $5.2 R_\odot$ , an outer radius of  $23 R_\odot$ , a maximum temperature of  $\simeq 14,000$  K, and a density of  $10^{-13}$  g cm $^{-3}$ , and for the stream they include initial/final velocities of 100/500 km s $^{-1}$ , an initial density of  $6 \times 10^{-14}$  g cm $^{-3}$ , a temperature of 8000 K, and a radius of  $4 R_\odot$ . A lower

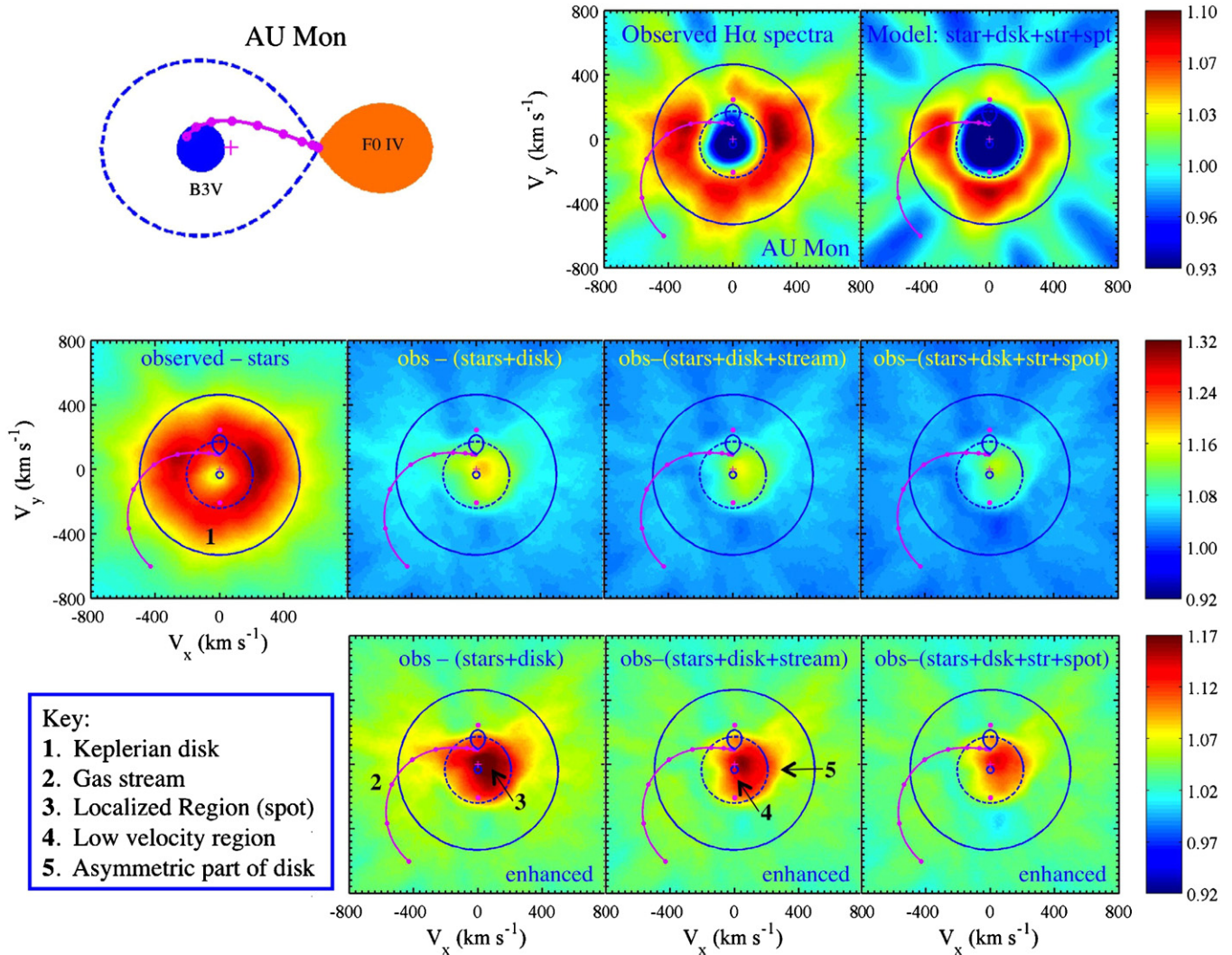


**Figure 12.** Two-dimensional Doppler tomograms obtained when the model fits for the various structures (stars, disk, stream, spot/localized region) are sequentially removed from observed spectra. This figure shows the Cartesian representation of the binary (top left), the observed and combined model tomograms (top right), the difference tomograms in sequence (middle frames) for (1) observed-stars, (2) obs-(stars+disk), (3) obs-(stars+disk+stream), and (4) obs-(stars+disk+stream+spot). The images for the latter three are enhanced in the bottom frames.

(A color version of this figure is available in the online journal.)

limit for the mass transfer rate was found to be  $\sim 2.4 \times 10^{-9} M_{\odot} \text{ yr}^{-1}$ .

3. We generate Doppler tomograms from the observed and difference spectra to investigate the 2D accretion structure in velocity space. Sequential removal of the stellar/disk/stream/spot components confirms the accuracy of the *Shellspec* modeling, and additionally identifies unmodeled aspects of the system. These include an asymmetric component of an elliptical accretion disk, and material moving at sub-Keplerian velocities that provides excess H $\alpha$  emission, plausibly associated with the continuation of the mass transfer stream beyond the splash site or perhaps a source of outflow or mass loss from the system.

We thank the referee for helpful comments on the manuscript and Kathryn Kreckel for obtaining MDM spectra of AU Mon over two nights. This research was partially supported by NSF grant AST-0908440 (M.T.R.) and NASA ADP grants NNG04GC48G and NNX12AE44G (G.J.P. and M.T.R.). The Hobby–Eberly

Telescope (HET) is a joint project of the University of Texas at Austin, the Pennsylvania State University, Stanford University, Ludwig-Maximilians-Universität München, and Georg-August-Universität Göttingen. The HET is named in honor of its principal benefactors, William P. Hobby and Robert E. Eberly. The Image Reduction and Analysis Facility (IRAF; <http://iraf.noao.edu/>) was used in this work, and the MATLAB software package was used to make the tomography images. The latest version of the *Shellspec* code can be obtained at <http://www.astro.sk/~budaj/shellspec.html>.

## REFERENCES

- Agafonov, M. I., Sharova, O. I., & Richards, M. T. 2009, *ApJ*, **690**, 1730  
 Ak, H., Chadima, P., Harmanec, P., et al. 2007, *A&A*, **463**, 233  
 Barai, P., Gies, D. R., Choi, E., et al. 2004, *ApJ*, **608**, 989  
 Barriá, D., & Mennickent, R. E. 2011, in ASP Conf. Ser. 447, Evolution of Compact Binaries, ed. L. Schmidtobreick, M. R. Schreiber, & C. Tappert (San Francisco, CA: ASP), 263  
 Bisikalo, D. V., & Kononov, D. A. 2010, *Mem. Soc. Astron. Ital.*, **81**, 187  
 Budaj, J. 2011a, *AJ*, **141**, 59  
 Budaj, J. 2011b, *A&A*, **532**, L12

- Budaj, J., & Richards, M. T. 2004, *Contrib. Astron. Obs. Skalnaté Pleso*, **34**, 167
- Budaj, J., Richards, M. T., & Miller, B. 2005, *ApJ*, **623**, 411
- Castelli, F., & Kurucz, R. L. 2003, in *IAU Symp. 210, Modelling of Stellar Atmospheres*, ed. N. Piskunov, W. W. Weiss, & D. F. Gray (San Francisco: ASP), A20
- Chadima, P., Fiřt, R., Harmanec, P., et al. 2011, *AJ*, **142**, 7
- Crawford, J. A. 1955, *ApJ*, **121**, 71
- Desmet, M., Frémat, Y., Baudin, F., et al. 2010, *MNRAS*, **401**, 418
- Djurašević, G., Latković, O., Vince, I., & Cséki, A. 2010, *MNRAS*, **409**, 329
- Gray, R. O., & Corbally, C. J. 1994, *AJ*, **107**, 742
- Ibanoglu, C., Dervishoglu, A., Cakirli, O., Sipahi, E., & Yuce, K. 2012, *MNRAS*, **419**, 1472
- Joy, A. H. 1942, *PASP*, **54**, 35
- Kopal, Z. 1955, *Ann. Astrophys.*, **18**, 379
- Kreiner, J. M. 2004, *Acta Astron.*, **54**, 207
- Lorenzi, L. 1980, *A&A*, **85**, 342
- Marsh, T. R., & Horne, K. 1988, *MNRAS*, **235**, 269
- Mennickent, R. E., Kołaczkowski, Z., Djurašević, G., et al. 2012, [arXiv:1205.6848](https://arxiv.org/abs/1205.6848)
- Mennickent, R. E., Kołaczkowski, Z., Graczyk, D., & Ojeda, J. 2010, *MNRAS*, **405**, 1947
- Mennickent, R. E., Kołaczkowski, Z., Michalska, G., et al. 2008, *MNRAS*, **389**, 1605
- Mennickent, R. E., Pietrzyński, G., Diaz, M., & Gieren, W. 2003, *A&A*, **399**, L47
- Miller, B., Budaj, J., Richards, M., Koubský, P., & Peters, G. J. 2007, *ApJ*, **656**, 1075
- Mimica, P., & Pavlovski, K. 2012, in *IAU Symp. 282, From Interacting Binaries to Exoplanets: Essential Modeling Tools*, ed. M. T. Richards & I. Hubeny (Cambridge: Cambridge Univ. Press), 63
- Olson, E. C., & Bell, D. J. 1989, *PASP*, **101**, 907
- Peters, G. J. 1989, *Space Sci. Rev.*, **50**, 9
- Peters, G. J. 1994, in *ASP Conf. Ser. 56, Interacting Binary Stars*, ed. A. W. Shafter (San Francisco, CA: ASP), 384
- Peters, G. J., & Polidan, R. S. 1982, in *IAU Symp. 98, Be Stars*, ed. M. Jaschek & H.-G. Groth (Dordrecht: Reidel), 405
- Peters, G. J., & Polidan, R. S. 1984, *ApJ*, **283**, 745
- Peters, G. J., & Polidan, R. S. 1998, *ApJ*, **500**, L17
- Peterson, W. M., Mutel, R. L., Lestrade, J.-F., Güdel, M., & Goss, W. M. 2011, *ApJ*, **737**, 104
- Plavec, M. J., & Polidan, R. S. 1976, in *IAU Symp. 73, Structure and Evolution of Close Binary Systems*, ed. P. Eggleton, S. Mitton, & J. Whelan (Dordrecht: Reidel), 289
- Raymer, E. 2012, *ApJ*, in press ([arXiv:1209.2167](https://arxiv.org/abs/1209.2167))
- Richards, M. T. 1992, *ApJ*, **387**, 329
- Richards, M. T. 2004, *Astron. Nachr.*, **325**, 229
- Richards, M. T., Agafonov, M. I., & Sharova, O. I. 2012, *ApJ*, **760**, 8
- Richards, M. T., & Albright, G. E. 1999, *ApJS*, **123**, 537
- Richards, M. T., Koubský, P., Šimon, V., et al. 2000, *ApJ*, **531**, 1003
- Richards, M. T., & Ratliff, M. A. 1998, *ApJ*, **493**, 326
- Richards, M. T., Sharova, O. I., & Agafonov, M. I. 2010, *ApJ*, **720**, 996
- Sahade, J., Ferrer, O. E., Garcia, L., Brandi, E., & Barba, R. H. 1996, *RevMexAA Conf. Ser.*, **4**, 109
- Sahade, J., Ferrer, O., Garcia, L. G., Brandi, E., & Barba, R. 1997, *PASP*, **109**, 1237
- Simon, V. 1998, PhD thesis, Charles Univ., Prague, Czech Republic
- Tkachenko, A., Lehmann, H., & Mkrtichian, D. E. 2009, *A&A*, **504**, 991
- Tkachenko, A., Lehmann, H., & Mkrtichian, D. 2010, *AJ*, **139**, 1327
- van Rensbergen, W., de Greve, J. P., Mennekens, N., Jansen, K., & de Loore, C. 2011, *A&A*, **528**, A16
- Vivekananda Rao, P., & Sarma, M. B. K. 1998, *A&AS*, **128**, 441
- Zavala, R. T., Hummel, C. A., Boboltz, D. A., et al. 2010, *ApJ*, **715**, L44